One-step aerosol synthesis of a double perovskite oxide ($KBaTeBiO_6$) as potential catalysts for CO_2 photoreduction

Journal:	*Nanoscale*
Manuscript ID	NR-ART-03-2021-001505.R1
Article Type:	Paper
Date Submitted by the Author:	12-May-2021
Complete List of Authors:	Zhou, Hao ; Washington University in St Louis, Energy, Environmental and Chemical Engineering Kouhnavard, Mojgan; Washington University in St Louis, Energy, Environmental and Chemical Engineering Jung, Sungyoon; Washington University in St Louis, Energy, Environmental and Chemical Engineering Mishra, Rohan; Washington University in St. Louis, Mechanical Engineering and Materials Science; Washington University in Saint Louis, Biswas, Pratim; Washington University in St Louis, Energy, Environmental and Chemical Engineering

One-step aerosol synthesis of a double perovskite oxide ($KBaTeBiO_6$) as potential catalysts for CO_2 photoreduction

*Hao Zhou, Mojgan Kouhnavard, Sungyoon Jung, Rohan Mishra, and Pratim Biswas**

H. Zhou, Dr. M. Kouhnavard, Dr. S. Jung, Prof. P. Biswas
Aerosol and Air Quality Research Laboratory, Department of Energy, Environmental and Chemical Engineering, Washington University in St. Louis, St. Louis, Missouri 63130, USA
E-mail: pbiswas@wustl.edu

Prof. R. Mishra
Institute of Materials Science & Engineering, Washington University in St. Louis, St. Louis, Missouri 63130, USA

Keywords: lead-free perovskites, aerosol-route synthesis, furnace aerosol reactor, nanoparticles, CO_2 photoreduction

This study presents a comprehensive investigation on the aerosol synthesis of a semiconducting double perovskite oxide with a nominal composition of $KBaTeBiO_6$, which is considered as a potential candidate for CO_2 photoreduction. We demonstrate the rapid synthesis of the multispecies compounds $KBaTeBiO_6$ with extreme high purity and controllable size through a single-step furnace aerosol reactor (FuAR) process. The formation mechanism of the perovskite in the aerosol route is investigated using thermogravimetric analysis to identify the optimal reference temperature, residence time and other operational parameters in the FuAR synthesis process to obtain the highly pure $KBaTeBiO_6$ nanoparticles. It is observed that particle formation in the FuAR is based on a mixture of gas-to-particle and liquid-to-particle mechanisms. The phase purity of the perovskite nanoparticles depends on the ratio of the residence time and the reaction time. The particle size is strongly affected by the precursor concentration, residence time and the furnace temperature. Finally, the photocatalytic performance of the synthesized $KBaTeBiO_6$ nanoparticles is investigated for CO_2 photoreduction under UV-light. The best performing sample exhibits an average CO production rate of 180 μmol g^{-1} h^{-1} in the first half hour with a quantum efficiency of 1.19%, demonstrating $KBaTeBiO_6$ as a promising photocatalyst for CO_2 photoreduction.

1. Introduction

The rapidly growing demand on clean energy and environmental protection has triggered the development of new materials with high catalytic performance for electro- or photo-reduction of greenhouse gases such as CO_2. Perovskites, with a stoichiometry of AMX_3, where A and M are cations and X is an anion, have long been recognized as catalysts with low cost and compositional flexibility.[1] However, they are known to exhibit insufficient activity and unsatisfactory stability.[2] Recently, double perovskites — that incorporate more than one element at either or both of the A and M cation sites and thus provide a large combinatorial space for tuning structure and properties — have been proposed as attractive alternatives to single perovskites showing better stability and performance, and demonstrating great potential for application as photovoltaics, electrocatalysts and photocatalysts.[2-4] The general formula for double perovskite is $A'A''M'M''X_6$, where A' and A'' are larger-sized cations, and M' and M'' are smaller-sized cations. $M'X_6$ and $M''X_6$ octahedra form a three-dimensional corner connected framework with the larger A' and A'' cations occupying the voids formed within the octahedral framework. X is commonly an oxide or halide ion. The broad diversity of chemical and physical properties of double perovskites is attributed to the possibility of various combination of A', A'', M' and M'' with different sizes and valences.[5-6] There are thousands of experimentally reported double perovskites,[7] with many more that have been predicted to be stable theoretically. However, most of them are difficult to synthesize and still remain to be produced and characterized.[8-9]

Double perovskites containing bismuth at either the one of the octahedral sites (M) are attractive as they offer a good combination of bandgap in the visible region to harness solar energy, stability, and are environmentally benign, as opposed to the popular lead-halide perovskites.[2, 10] They have been widely applied in catalytic CO_2 conversion to fuels using solar energy.[11-13] Cs_2AgBiX_6 with bandgaps range from 1.9 eV to 2.19 eV (X = Br) and 2.2 eV to 2.77 eV (X = Cl) were synthesized through both co-precipitation and solid state reaction routes.[14-16] Zhou et al.[11] prepared $Cs_2AgBiBr_6$ nanocrystals with an indirect bandgap 2.52 eV via a hot injection method, achieving a total electron consumption of 105 μmol g^{-1} over 6 h for CO_2 photoreduction. Other perovskites containing Bi at the *A*-site, such as Bi_2WO_6 and Bi_2MoO_6, have also been explored for CO_2 photoreduction. Sun et al.[12] reported ball-flower-like Bi_2WO_6 with an experimental bandgap 2.63 eV by a hydrothermal method, exhibiting CO yield of 2.5 μmol g^{-1} in 5 h. Bi_2MoO_6 microspheres were fabricated via a facile hydrothermal approach by Dai et al..[13] The production rates of methanol and ethanol are 6.2 μmol g^{-1} h^{-1} and 4.7 μmol g^{-1} h^{-1}, respectively. However, the reported photocatalytic activities of all the Bi-based compounds are below that of other advanced catalysts, such as gas synthesized Pt-TiO_2 thin films having a CH_4 yield of 1361 μmol g^{-1} h^{-1}.[17] Recently, Thind et al.[9] employed density-functional-theory (DFT) calculations and materials informatics to predict a stable bismuth-containing oxide double perovskite $KBaTeBiO_6$, from a vast composition space of over 29,000 $A'A''M'BiO_6$ theoretical compounds. In contrast to most oxides that show wide band gaps, $KBaTeBiO_6$ was predicted to have a band gap of 1.94 eV and low effective mass of the charge carriers, which make it a promising catalyst for CO_2 photoreduction. This new compound was subsequently synthesized using the conventional wet-chemistry method and showed an experimental band gap of 1.88 eV and excellent stability under ambient conditions. However, the as-prepared perovskite by this simple shake and bake method exhibited impurity phases and had large particle sizes, which are expected to result in a low photocatalytic efficiency. In addition, a very long time for both reaction and post-treatment also limits its large-scale application. Therefore, to realize the potential of $KBaTeBiO_6$ double perovskites for CO_2 photocatalysis and large-scale production, a rapid and continuous method to synthesize highly crystalline and phase pure nanoparticles of this compositionally complex material, with controllable size and improved physicochemical properties is highly desirable.

There are a number of methods that can be used to fabricate perovskite materials apart from the conventional wet-chemistry method,[9] such as solid state reaction,[18] hydrothermal/solvothermal synthesis,[19] sol-gel[20] , and aerosol synthesis[21,22]. Among these methods, aerosol spray pyrolysis has emerged as a popular route for the preparation of perovskites. Compared to other synthesis techniques, it has the following advantages: (1) simple and continuous operation; (2) high purity of the synthesized material; (3) short time to obtain the final product; (4) controllable size from micrometer to nanometer and ability to tune the morphology, and (5) excellent control of chemical uniformity and stoichiometry in multi-component systems.[23] Thus, the aerosol spray route is well suited for the synthesis of nanoparticles of compositionally complex double perovskites.

To overcome the limitations and challenges in synthesizing multicomponent perovskite materials, we report herein an innovative rapid and continuous aerosol synthesis of phase pure perovskite nanoparticles with nominal formula $KBaTeBiO_6$ with controllable nanometer sizes in a furnace aerosol reactor (FuAR). The operating conditions of this well controlled process are established to obtain the desired functional material in a single step. First, the reference temperature and residence time for the formation of the perovskite phase in FuAR were carefully evaluated based on the decomposition characteristics of a mixture of nitrate salts, which were studied by thermogravimetric analysis (TGA). Then a series of oxide perovskite powders were synthesized via one-step FuAR by controlling the operation parameters, such as the furnace temperature, the aerosol flow rate, and the precursor component concentration. The as-prepared nanoparticles were characterized in detail to relate its properties to processing conditions. Particular attention is paid to phase purity and the size of the nanomaterials. The phase pure nanoparticles were only found under a specific combination of operating conditions (barium concentration: 0.025 M, K:Ba:Te:Bi=1:1:1:0.8, furnace temperature:900 °C, the aerosol flow rate: 1.8 L min^{-1}). Particle sizes less than 100 nm could be readily produced. The detailed analysis of the perovskite formation mechanism in the aerosol route can be very helpful for the future synthesis of other multispecies perovskites with high purity. Finally, the photocatalytic performance of the new perovskite was tested for CO_2 reduction, achieving 180 μmol g^{-1} h^{-1} in the first half hour, much higher than that of most oxide perovskites reported in literature.

2. Experimental Section

2.1 Precursor solution preparation

In this experiment, a mixture of cost-effective nitrate salts was used as the precursor. Potassium nitrate (KNO_3), barium nitrate ($Ba(NO_3)_2$), telluric acid ($Te(OH)_6$), and bismuth nitrate pentahydrate ($Bi(NO_3)_3{\cdot}5H_2O$) were purchased from Sigma-Aldrich (St. Louis, MO) and used as raw materials for the cation sources. All reagents are commercial materials of reagent grade and were used without further purification. All the cation sources, except for bismuth, were prepared by dissolving its corresponding reagent separately into deionized water (DI water). For the bismuth precursor, $Bi(NO_3)_3{\cdot}5H_2O$ was dissolved in a mixture of nitric acid (HNO_3, Sigma-Aldrich) and DI-water (1:7 ratio of HNO_3/H_2O). Then all precursors were mixed in DI water while stirring. Due to the different solubilities of these chemicals in acid, there exists a very narrow pH window, only within this range all chemicals can be dissolved. HNO_3 was added to the mixture to modify pH value between 0 to 1, so that a transparent and stable solution was obtained for further spraying.

2.2 Phase formation experiments by TGA

The mechanism for the formation of $KBaTeBiO_6$ and the kinetics of the pyrolysis of a mixture of nitrate salts were studied using a TGA (TA Instruments, New Castle, DE). The precursor solution (0.025 M equimolar concentration) was firstly allowed to dry at 100 °C for 24 hours. The dried precursor was later ground to obtain a uniform material. Samples of 20 mg were used for each run and all experiments were carried out with a flow of air of 25 mL min^{-1} to maintain the oxidative environment. The thermogravimetric (TG) and differential thermogravimetric (DTG) curve were recorded at heating rates of 10, 20, 50 and 100 °C min^{-1} from room temperature to 900 °C. According to the TGA results, kinetic parameters, such as the activation energy, reaction order and pre-exponential factor were calculated by the Coats-Redfern approximation method.[24]

2.3 Synthesis of $KBaTeBiO_6$ nanoparticles in the furnace aerosol reactor

The $KBaTeBiO_6$ nanoparticles were synthesized using a single-step furnace aerosol reactor. Figure 1 shows a schematic diagram of the experimental set up used in this study. The concentration of each cation in the precursor solution was set from 0.01 to 0.05 M in all experiments. The solutions were atomized into fine aerosol droplets by using a Collison nebulizer and delivered by air to the furnace aerosol reactor with a flow rate ranging from 0.9 L min^{-1} to 4.5 L min^{-1}. A home-built diffusion drier was used to promote the complete evaporation of solvent before entering the furnace. The pyrolysis furnace (1 m long × 25 mm ID) was programmed between 650 °C and 1000 °C, where dried precursor particles undergo decomposition and reaction to form the final perovskites. The resulting powders were collected on a glass fiber membrane filter. A portion of the aerosol flow at the end of the furnace tube was sampled and analyzed by a scanning mobility particle sizer to obtain the particle size distribution in real-time.

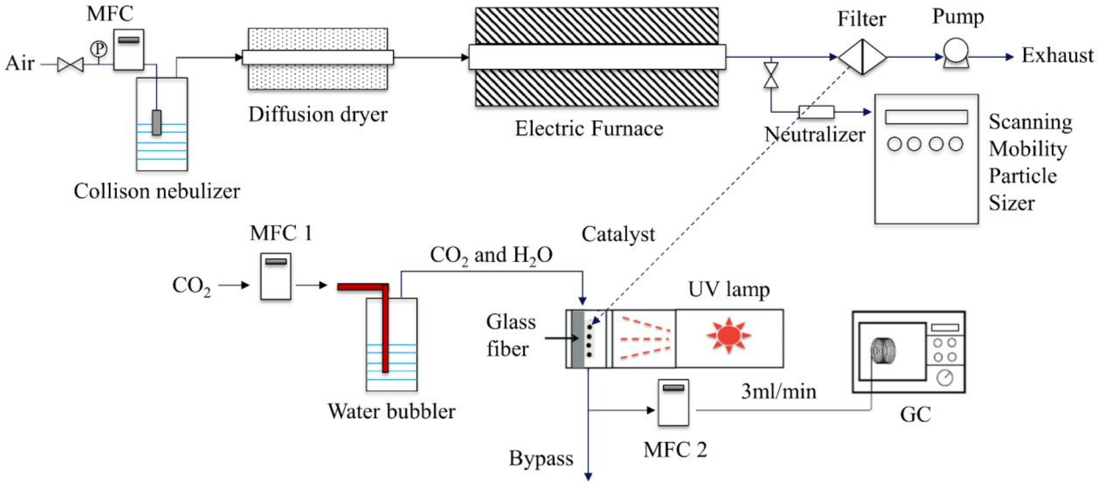

Figure 1. Schematic diagram of the furnace aerosol reactor and CO_2 photoreduction system

2.4 Characterization of $KBaTeBiO_6$ powder

The crystal structure of the fabricated powder was examined by X-ray diffraction (XRD, D8 Advance, Bruker, USA) with a Cu Kα radiation source, which is operated at 40 keV and 40 mA. The measurement was performed in 2θrange of 10 – 60 degree at a step size of 0.02°. TOPAS 4.2 software was used for Rietveld refinement. The morphology of samples was characterized through transmission electron microscopy (TEM, FEI Tecnai G2 Spirit) at an accelerating voltage of 120 kV. The UV-vis spectrum was recorded through a UV−vis spectrophotometer (UV-2600, Shimadzu, USA). The valence band, conduction band and Fermi level position were determined by performing ultraviolet photoemission spectroscopy (UPS, 5000 VersaProbe II) measurements. The chemical composition of the powder samples was analyzed by inductively coupled plasma-optical emission spectroscopy (ICP-OES, PerkinElmer: Optima 7300DV). The surface chemistry was characterized by X-ray photoelectron spectroscopy (XPS, PHI 5000 VersaProbe II).

A scanning mobility particle sizer (SMPS, TSI Inc.) was used to measure the size distribution of as-fabricated samples. SMPS includes a differential mobility analyzer (DMA, model 2081, TSI Inc.) for particle size classification and a condensation particle counter (CPC, model 3010, TSI Inc.) for particle number counting. In this system, the aerosol was firstly neutralized by a radioactive source to obtain a known equilibrium charge distribution. These particles were then introduced into the DMA and classified depending on their electrical mobility. CPC was employed to count the number of particles with a specific electrical mobility.

2.5 CO_2 photoreduction experiments

CO_2 photoreduction experiments were performed in a continuous flow reactor with a cylindrical-shaped reaction cell, which is described in our previous publications[17, 25-27] in detail. For each test, the glass filter loaded with powder samples is placed in the reaction cell with a quartz window allowing the incidence of light. A mixture of CO_2 and H_2O was generated through DI water bubbled by a compressed CO_2 with high purity (99.999%). Then the gas mixture was continuously introduced to the reaction chamber as reactants. Before irradiation, the reactor system was purged with CO_2 and H_2O for 1 hour at a high flow rate of 100 ml min^{-1} to make sure there were no air and carbon residue. Then the flow rate was fixed at 20 ml min^{-1} and the light source was switched on for the whole 3h analysis. Here a Xe arc lamp (Oriel 66021, Newport Co.) operated at 400 W without a filter was used to provide light, which has an accumulated intensity of 3.6 mW cm^{-2} in an effective UV range of 250-354 nm. During the experiments, 3 ml min^{-1} of effluent gases was sampled from the reaction cell at a given time interval and analyzed by a gas chromatograph (GC, 6895N, Agilent Technologies, Inc.). The GC was equipped with a thermal conductivity detector (TCD), using Helium as the carrier gas. The product yield was calculated based on the flow rate, catalyst mass and irradiation time. Control tests were conducted under the following three conditions: (1) glass filter without catalysts; (2) no light illumination; (3) no CO_2 and H_2O.

An overall experimental plan in this study is given in Table 1.

Table 1. Experimental plan

Test #	Objective	Instruments used	Description
1	Perovskite phase formation mechanism	TGA, XRD	Study the reaction mechanism and kinetic of $KBaTeBiO_6$ formation from a mixture of the nitrate salts under different heating rate: 10, 20, 50, 100 °C /min
2	The synthesis of $KBaTeBiO_6$ in FuAR and characterization	XRD, TEM, SMPS, ICP-OES, UV-vis	Optimize the operation parameters to obtain nanosized perovskite nanoparticles with high purity. (1) Furnace temperature: 650-1000°C ; (2) Precursor concentration: 0.01-0.05 M; (3) The aerosol flow rate: 0.9-4.8 LPM; (4) Precursor element ratio: K:Ba:Te:Bi =1:1:1:1, 1:1:1:1:0.8
3	The performance of $KBaTeBiO_6$ for CO_2 photoreduction	CO_2 photoreduction analysis system	(1) Confirm that carbon containing products resulting from the reaction of CO_2 and water vapor; (2) Evaluate the catalytic performance of phase pure powders for CO_2 photoreduction

3. Results and Discussion

3.1 Formation mechanism of $KBaTeBiO_6$ nanoparticles

A deep understanding of the mechanism for the formation of the perovskite phase is tantamount for the optimization of synthesis processes in FuAR. In this study, $KBaTeBiO_6$ formation was studied by TGA on powder samples resulting from complete drying of 0.025 M equimolar precursors. Figure 1a shows the thermal analysis of dried samples under heating rate 10 °C min^{-1}. Four stages can be observed during the perovskite formation process. XRD data was provided at each stage. Figure S1 shows the XRD patterns at 260, 490 and 600 °C, which correspond to the second, third and fourth stage, respectively. In the first stage (0 - 160 °C), the weight loss is around 5%, which is normally attributed to the evaporation of absorbed water molecules. In the second stage (160 - 260 °C), bismuth potassium dioxide dinitrate ($Bi_{1.7}K_{0.9}O_2(NO_3)_2$) is generated, which indicates the $Ba(NO_3)_3$ may decompose and react with KNO_3 to form new compound resulting in a weight loss of 10.3%. Bismuth oxides are produced in the third stage, which lead to a weight loss of 5.5% from 260 °C to 490 °C. In the fourth stage (490 - 690 °C), barium nitrates decompose and react with other metal salts to form the perovskite phase. The remaining mass is around 62.8 wt%, which agrees well with the calculated ratio 61.7% of the molecular weights of $KBaTeBiO_6$ and initial salts.

The effect of the heating rate on the formation process was also investigated. As shown in Figure 2a, a similar TGA curve was observed for mixed nitrate salts at a higher heating rate of 100 °C min^{-1}. It can be observed that higher heating rates results in higher decomposition temperatures. In addition, at a heating rate of 100 °C min^{-1}, the remaining mass after the fourth stage was at ~61.6% of the original mass, suggesting that a small amount of evaporation may have occurred. Zhang et al.[28] have reported a similar trend that increasing the heating rate promotes the evaporation of the metal salts. Therefore, when metal nitrates are exposed to high temperatures, there exists a competition between the evaporation and decomposition of the metal salts, which depends on the heating rate, temperature, and the properties of the nitrates.

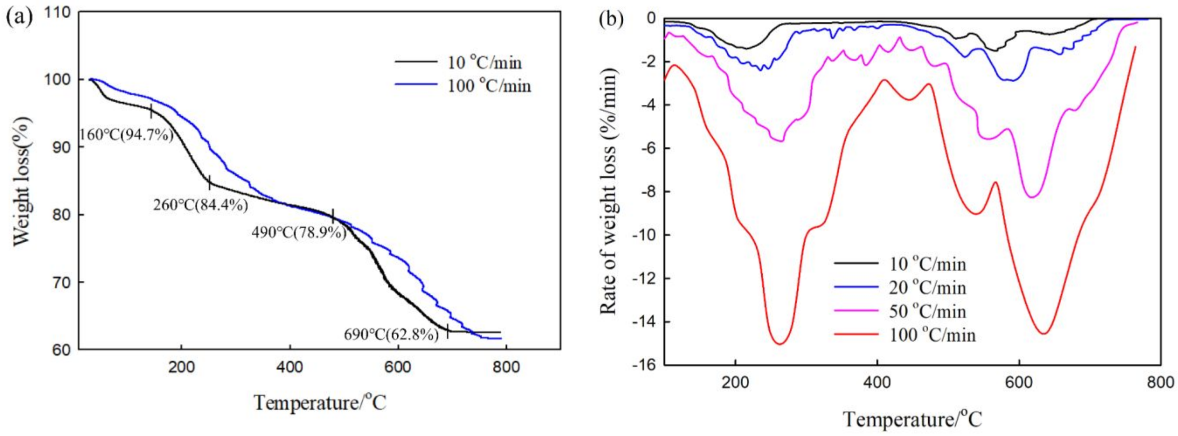

Figure 2. a) Thermogravimetric analysis of 0.025 M equimolar precursors under the heating rate of 20 and 100 °C min^{-1}; b) DTG curves of 0.025 M equimolar precursors decomposition at a heating rate of 10, 20, 50 and 100 °C min^{-1}

Figure 2b shows the derivative thermogravimetric (DTG) curve of the dried precursor at the heating rates of 10, 20, 50 and 100 °C min^{-1} in air environment. There are two main peak temperatures for each DTG curve, which correspond to the highest decomposition rate at the second and the fourth stages. As the heating rate increases, the decomposition rate shifts to a higher value. The peak temperature in the fourth stage increased from 567 to 637 °C.

The kinetic parameters can be derived based on the non-isothermal TGA curves. The general kinetic equation is expressed as:

$$\frac{d\alpha}{dt} = Aexp\left(-\frac{E}{RT}\right)(1-\alpha)^n \qquad (1)$$

where α is the conversion degree, t is time, A is pre-exponential factor, E is the energy of activation, R is the universal gas constant, T is the temperature, n is the reaction order. The Coast and Redfern approximation method[24] was used to determine the apparent activation energy, reaction order and frequency factor in each decomposition stage. The detail of this methodology is described in the Supporting Information. We assume that the kinetic parameters are constants under different heating rate. Then, the energies of activation were calculated as

79.28±2.77 kJ mol^{-1}, 63.53±2.27 kJ mol^{-1}, and 147.31±7.61 kJ mol^{-1} for the second, third, and fourth steps, respectively. The kinetic parameters for various steps are summarized in Table 2.

Table 2. Kinetic parameters of 0.025 M equimolar precursor

Stage	E (kJ mol^{-1})	n	ln A (1 min^{-1})
Second stage	79.28±2.77	1	18.80±1.20
Third stage	63.53±2.27	2.1	11.47±0.21
Fourth stage	147.31±7.61	1.6	19.67±1.39

In FuAR, the heating rate is ~10,000 °C min^{-1} at the inlet of the furnace tube. In order to make sure all precursors fully decompose to corresponding oxides and then form the perovskite, it is necessary to set the furnace temperature larger than the peak temperature of the last decomposition process at 10,000 °C min^{-1}. Based on the Kissinger method,[29] the peak temperature under 10,000 °C min^{-1} in the last decomposition stage is calculated as 971 °C, which provides a reference temperature to set the furnace. Under the constant temperature of 971 °C, the time required for the decomposition of nitrate salts and the reaction of mixed oxides to form perovskite is 10.8 s, which provides the reference residence time. It should be noted that this is a qualitive analysis, where the effects of particle size and evaporation on the perovskite formation have been neglected. However, in aerosol spray pyrolysis, the particle size is normally sub micrometer, much smaller than the bulk size. The evaporation may also become significant due to the high heating rate and thus cannot be disregared,[28] which leaves room for further optimization in the future. Based on the reference temperature and residence time, the furnace temperature can be varied from 650 to 1000 °C. The residence time is set on the order of one second.

Based on the TGA results, we can see that the synthesis of $KBaTeBiO_6$ in the furnace aerosol reactor may involve not only the droplet-to-particle process but also the gas-to-particle process due to the evaporation of nitrate salts under a high heating rate. In our experiments, the primary droplets form in the aerosol generator and then pass through the diffusion dryer, where the solvent evaporates completely, leaving behind only the metal nitrates remaining in the droplet.

From the diffusion dryer, the precursor particles enter the furnace reactor. Three possible particle formation mechanisms for spray pyrolysis have been proposed,[30,31] as seen in Figure 3. The first mechanism is the liquid-to-particle conversion, wherein the precursors completely decompose to their corresponding oxides and there is no vaporization. In this case, one droplet leads to one large particle. The second mechanism is the gas-to-particle conversion, where the precursors undergo complete evaporation to form vapors. Then the precursor vapors undergo nucleation, condensation, and coagulation to generate the aggregated particles.[32] The third mechanism is a mixture of the two mechanisms described above. When the precursor droplet is suddenly subjected to a very high temperature, the precursors can be vaporized before they decompose. In this case, some of the precipitates could be vaporized rather than decomposed to metal oxides. Then, at high temperature precursor vapors turn into small particles. This case is most likely to happen in FuAR due to its extreme high heating rate, which is confirmed in the next section.

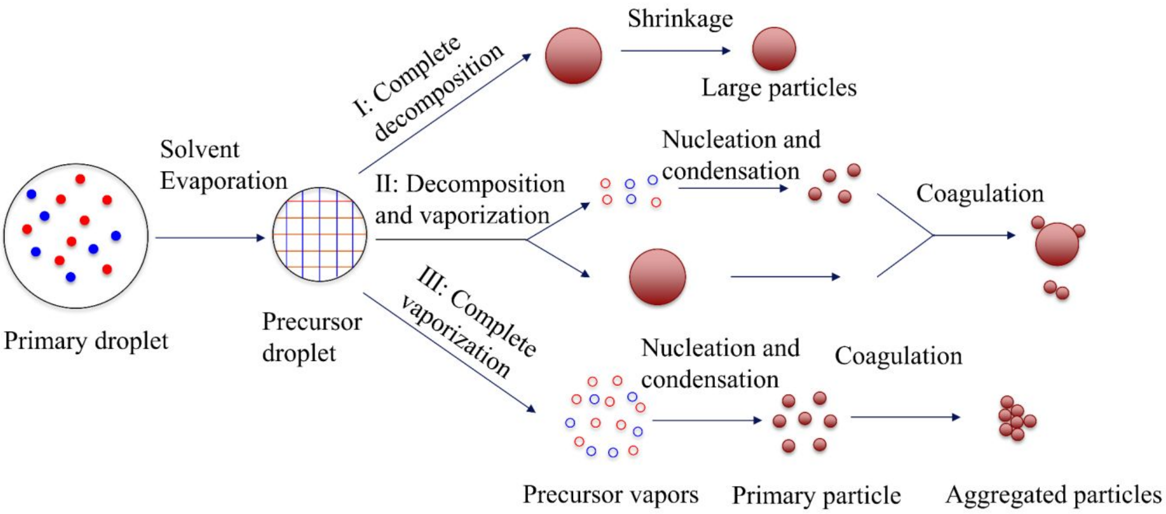

Figure 3. Particle formation mechanisms

3.2. The synthesis of $KBaTeBiO_6$ in FuAR

In this section, we discuss the optimization of the synthesis process to obtain the pure perovskite phase. The crystal structure and phase composition of perovskite oxide $KBaTeBiO_6$ fabricated by the one-step FuAR were investigated using XRD. Figure 4a shows the XRD results of samples grown under different temperatures. The precursor component concentration and the aerosol flow rate are fixed at 0.025 M, and 1.8 L min^{-1}, respectively. The precursor is equimolar. Figure 4a also includes the simulated Bragg position of $KBaTeBiO_6$ as a reference. Apart from the sample synthesized under 650 °C, all results show major diffraction peaks at 29.71°, 42.52°, and 52.74° that correspond to (020)/(112), (004)/(220), and (024)/(132) planes of perovskites, respectively. Therefore, the creation of the perovskite phase occurs at 750 °C. Below 750 °C, the amount of perovskite phase is not significant enough, while the secondary phase was promoted above 950 °C. It indicates that there exists a narrow temperature window, within which the powders show an overwhelming perovskite phase. However, only the sample synthesized under temperature 900 °C exhibited minimum impurities. The influence of the temperature on phase purity for the precursor concentration of 0.01 M is also investigated. The results are shown in the Supporting Information (see Figure S2).

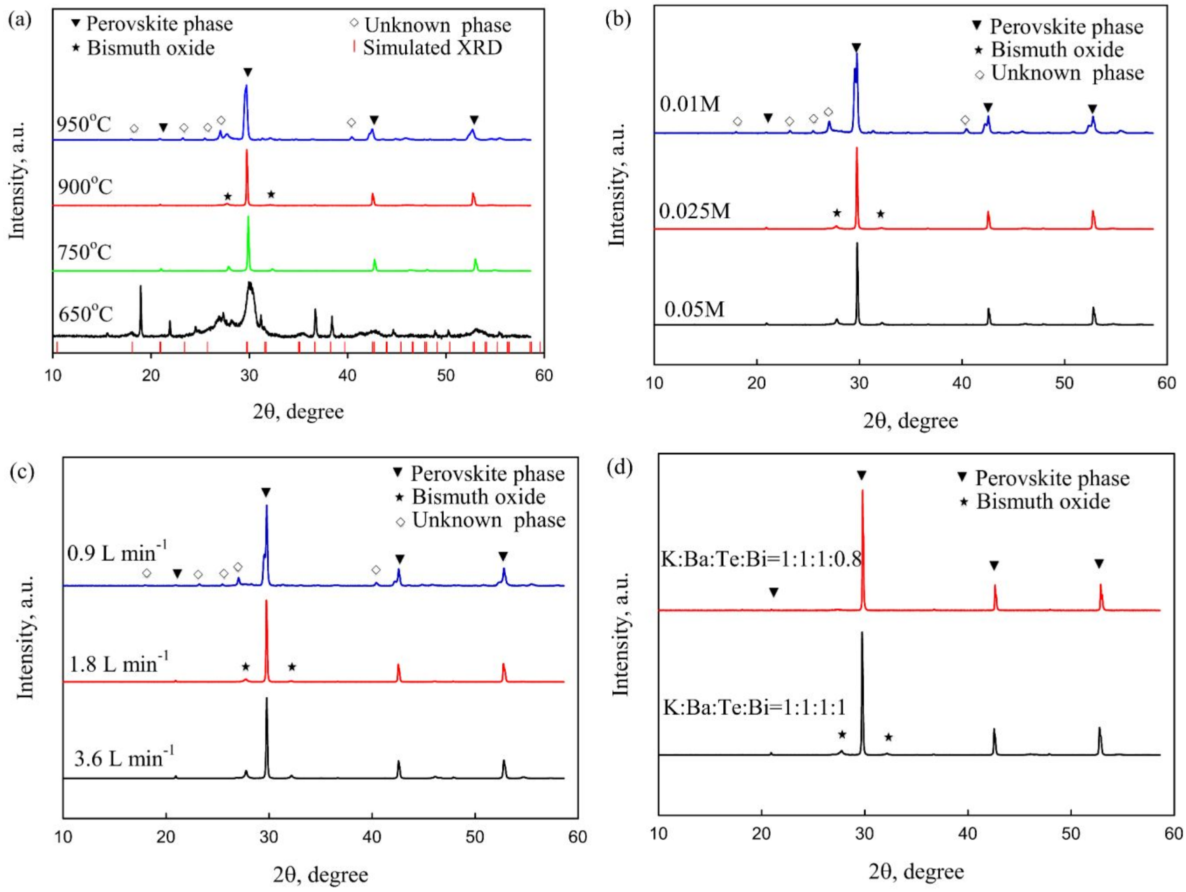

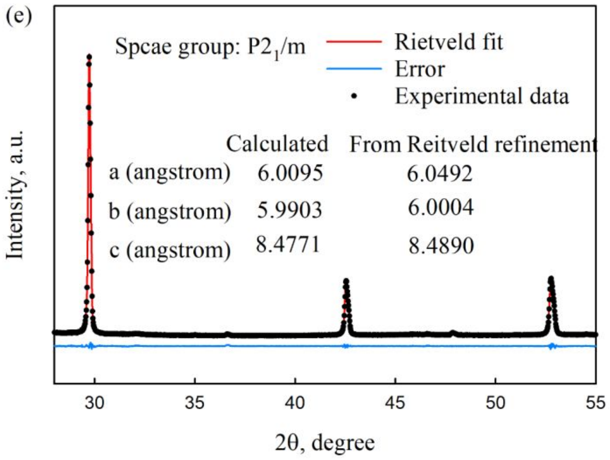

Figure 4. Particle XRD patterns of $KBaTeBiO_6$ under a) different temperatures (0.025 M, equimolar, 1.8 L min^{-1}); b) different concentrations (equimolar, 900 °C, 1.8 L min^{-1}; c) different flow rates (0.025 M, equimolar, 900°C); d) different elemental ratios (0.025 M, 900 °C, 1.8 L min^{-1}); e) Rietveld refinement of the experimental XRD data for phase pure $KBaTeBiO_6$ and the quality of the fit

The effects of the precursor concentration on the phase purity are shown in Figure 4b. The temperature is fixed at 900 °C and the flow rate is fixed at 1.8 L min^{-1}. The precursor is equimolar. It was observed that the sample showed the minimum impurities for the precursor concentration of 0.025 M. Decreasing or increasing the concentration from this optimal value resulted in an increase in the impurities. However, it should be noted that the impurity in samples prepared at the concentration of 0.05 M and 0.025 M both corresponds to bismuth oxides, while the impurity in the sample prepared for 0.01 M precursor is an unknown secondary phase.

Figure 4c shows the XRD pattern of samples synthesized under different aerosol flow rates ranging from 0.9 L min^{-1} to 3.6 L min^{-1}. The temperature and concentration are fixed at 900 °C and 0.025 M, respectively. The sample with minimum impurities was found at the flow rate of 1.8 L min^{-1}. Increasing the flow rate leads to an increase in the fraction of bismuth oxide phase, while decreasing the flow rate results in the appearance of a secondary phase.

In fact, the phase purity depends on the ratio of the reaction time τ_r of mixed oxides and the residence time τ_{res}. When τ_{res} is on the same order of τ_r, all solutes react to form the perovskite structure with little impurities. If τ_{res} is far smaller than τ_r, a part of the solutes does not participate in the reaction and remain as the impurity phase. If τ_{res} is far larger than τ_r, a secondary phase is promoted. In the furnace aerosol reactor, the residence time τ_{res} is calculated according to Equation 2 assuming the temperature is uniform:[33]

$$\tau_{res} = \frac{\pi D^2 L}{4Q}\left(\frac{T_0}{T}\right)\left(\frac{1-y_w}{1-y_w^0}\right) \tag{2}$$

where D is the diameter of the tube, L is the length of the tube, Q is the volume flow rate, T and T_0 are room temperature and tube temperature, respectively. y_w is the molar fraction of water vapor in air. The reaction time τ_r of mixed oxides is calculated by:

$$\tau_r = A^{-1}\exp\left(\frac{E}{RT}\right)\int_0^{0.99}(1-\alpha)^{-n}d\alpha \tag{3}$$

where E and n are 147.31 kJ mol^{-1} and 1.6 according to the kinetic parameters of fourth stage in TGA curve. A is an adjustable parameter to fit the experimental data obtained from the synthesis of perovskite in FuAR. If we assume $\tau_r = \tau_{res}$ for 0.025 M equimolar precursor at 900 °C and 1.8 L min^{-1}, then A=5.6×10^8 min^{-1}.

τ_r and τ_{res} can be determined using Equation 2 and 3 for all experimental conditions, which are listed in Table S1. From this table, we can find that below 900 °C, τ_{res}/τ_r is smaller than 1. Part of the precursors remains as impurities. Above 900 °C, τ_{res}/τ_r is larger than 1, promoting the formation of the secondary phase. Increasing the flow rate decreases the residence time. As a result, the precursor does not have enough time for the complete transformation into perovskite oxides, which causes more impurities. But further decreasing the flow rate increases the residence time, leading to the appearance of a secondary phase. Because Equation 3 does not account for the effects of the precursor concentration, the reaction time for different concentrations is the same. However, the influence of the concentration on the reaction time may be significant. For the precursor concentration of 0.05 M, it needs a longer time to completely transform all metal salts into perovskite oxides, due to ineffective heat transfer of the larger particles. Thus, under the same residence time, more impurity phase appeared for the concentration of 0.05 M. In contrast, for the precursor concentration of 0.01 M, it needs shorter time for the complete reaction. Although the impurity of bismuth oxide disappeared, relative long residence time to reaction time promotes the appearance of the secondary phase.

Until now, the best conditions for a 0.025 M equimolar precursor are 900 °C and 1.8 L min^{-1}. But samples under this condition still contained small number of impurities, which are not desirable for further application. From the XRD pattern, this impurity phase was identified as bismuth oxide. In order to further decrease the number of impurities, the bismuth concentration in the precursor was lowered to 0.02 M while the concentrations of other three elements were kept at 0.025 M. The XRD result after changing the element ratio of bismuth to barium is shown in Figure 4d. No additional impurity peaks were detected, implying a high purity of the perovskite oxide. Figure 4e presents the Rietveld refinements of the XRD pattern for the phase-pure powders. The space group is $P2_1/m$. The experimental lattice constants are a = 6.0492 Å, b = 6.0004 Å, c = 8.4890 Å, which are very close to calculated values (a = 6.0095 Å, b = 5.9903 Å, c = 8.4771 Å) by DFT.

ICP-OES was used to measure the actual cation ratio. The mass concentration of each element was converted to the molar ratio based on the barium concentration. The measured values for all samples are listed in Table S2. Results show that the stoichiometry ratio for all powders is not same as the nominal ratio 1:1:1:1. There is less potassium and more barium, which was also observed for powders synthesized by the wet-chemistry method.[9] This is understandable due to the difference in the decomposition and evaporation kinetics among the different nitrate salts. The amount of loss of each element is closely related to their vapor pressure. The higher the vapor pressure of a material at a given temperature, the faster the evaporation rate. Based on the literature, [34-37] barium, bismuth, tellurium and potassium compounds used have a vapor pressure of 63.3, 90.5, $4.0\times10^{4,}$ 3.5×10^{4} Pa at 900 °C, respectively. That is, the potassium precursor has the highest evaporation rate, whereas the barium nitrate has the lowest evaporation rate. This explains why there is more loss of potassium than barium. Figure 5a shows the influence of temperature on the elemental ratio for the 0.025 M equimolar precursor. With increasing temperature, Te/Ba and Bi/Ba decrease firstly and then increase. The results indicate that below 900 °C, the evaporation rates of bismuth and tellurium salts increase more rapidly than that of barium as the temperature goes up. However, above this temperature, the evaporation rate of barium salts becomes more sensitive to temperature and increases sharply, which results in an increased loss of barium. From Figure 5a, we can also see that K/Ba shows an overall decreasing trend with an increase in temperature, which shows the faster evaporation rate of potassium salts compared to that of barium salts.

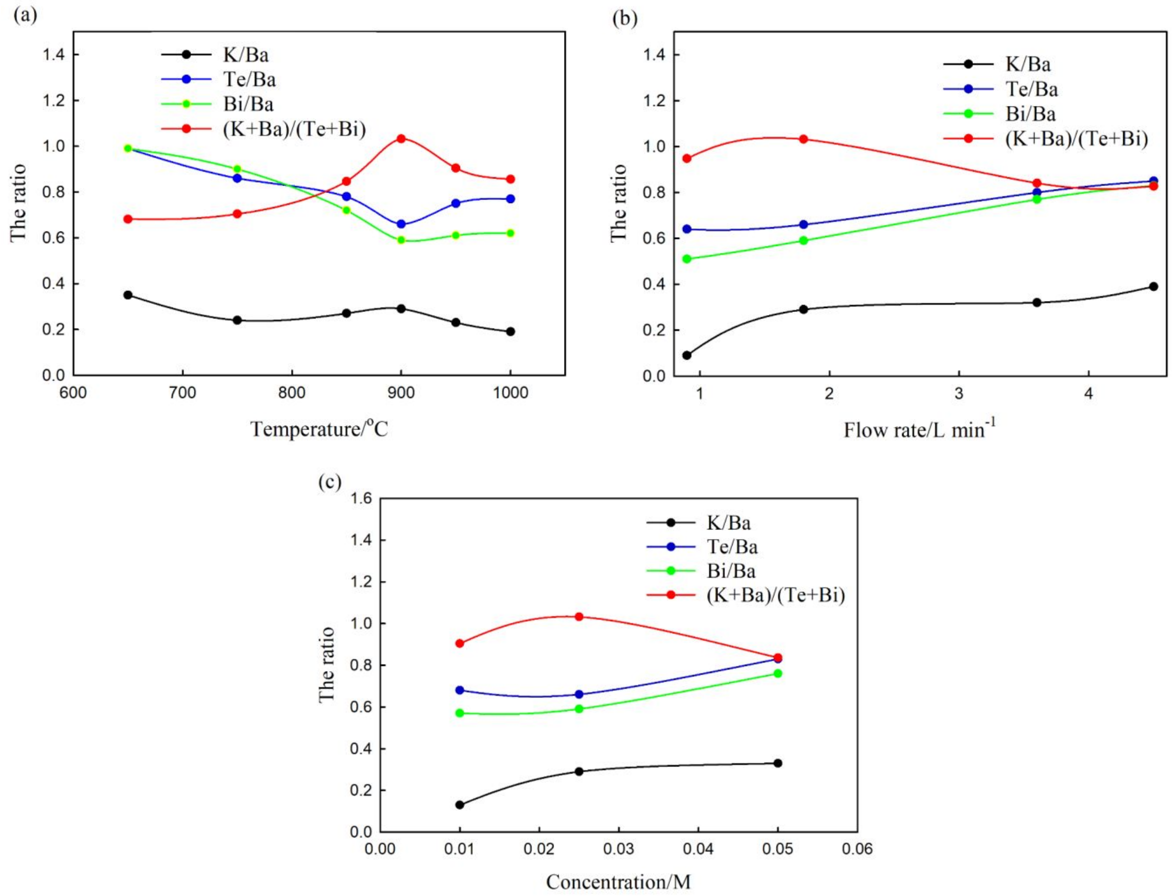

Figure 5. Particle formation mechanisms Elemental ratios of nanoparticles synthesized by FuAR under a) different temperatures (0.025 M, equimolar, 1.8 L min^{-1}); b) different flow rates (0.025 M, equimolar, 900 °C); c) different concentrations (equimolar, 900 °C, 1.8 L min^{-1})

The effects of the aerosol flow rate on the elemental ratio are presented in Figure 5b. It shows that K/Ba, Te/Ba, Bi/Ba all increase with increasing the aerosol flow rate. The reason is that increasing the aerosol flow rate decreases the residence time, which leads to increased amount of mass of K, Te, Bi compared to that of Ba due to the slower evaporation of Ba. Increasing concentration also increases the elemental ratio of Te/Ba, Bi/Ba and K/Ba, as seen in Figure 5c. It is noted that in all these figures, the ratio of *A* sites (K and Ba) and *M* sites (Te and Bi) has a maximum value 1.03 at a temperature of 900 °C and flow rate of 1.8 L min^{-1} for 0.025 M equimolar precursors. From the XRD results, we know this condition corresponds to the sample with minimum impurities. This is as expected that when *A*/*M* is around 1, an overwhelmingly perovskite phase can be formed. If *A*/*M* is far smaller or larger than 1, a significant secondary phase will appear.

SMPS was used to measure the particle size distribution of the as-synthesized perovskites under different experimental conditions. Figure 6a shows the influence of the temperature on the nanoparticle size distribution for 0.025 M equimolar precursors. The furnace temperature was changed from room temperature to 1000 °C. We can see that at room temperature, the size distribution is broad, and the particle has a geometric mean diameter (GMD) of 78 nm. In this case, nanoparticles are formed resulting from the complete evaporation of droplets without further decomposition or sintering. One droplet leads to one spherical solid particle. Based on the mass balance, the initial droplet size can be calculated using the following equation:[38]

$$d_0 = d_f \left(\sum_i^n \frac{C_i M_{wi}}{\rho_i} \right)^{-\frac{1}{3}} \tag{4}$$

where d_0 is the initial droplet diameter, d_f is the final particle size, C_i, M_{wi} and ρ_i are the concentration, molecular weight and density of species *i*, respectively

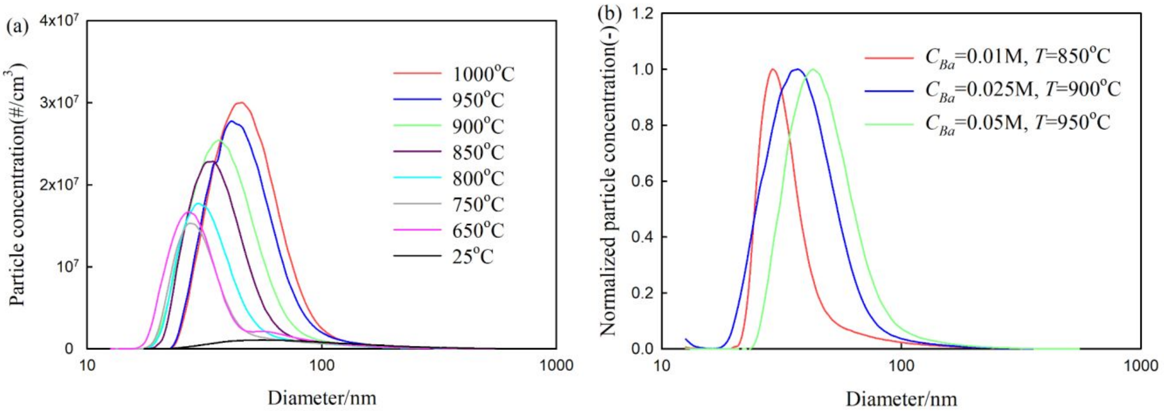

Figure 6. The particle size distribution of a) perovskite oxides synthesized at different temperatures (0.025 M, equimolar, 1.8 L min^{-1}) b) perovskite oxides with high purity synthesized at different experimental conditions (K:Ba:Te:Bi=1:1:1:0.8, aerosol flow rate: 1.8 L min^{-1})

According to Equation 4, the geometric mean diameter of droplets generated by our home-made Collison nebulizer is estimated as 390 nm. When the furnace temperature was increased to 650 °C, the size distribution became bimodal, with one peak around 70 nm, and the second peak centered at 25 nm. The total number concentration increased by more than 6 times compared to that at room temperature. This is attributed to a mixture of gas-to-particle and droplet-to-particle conversion. Dry nanoparticles entered the furnace from the diffusion dryer and were suddenly subjected to a high temperature. The nitrate salts evaporate partially before decomposition. The vapor mixture of precursors then undergoes homogeneous nucleation to form new particles. Therefore, the total number concentration increased, and a new peak appeared at small particle size. At the same time, the peak at large diameter shifts to left due to the evaporation and decomposition of nitrate salts. Upon further increasing the furnace temperature, the number concentration of small particles increased dramatically, and the peak at large size continued shifting to smaller sizes, which finally leads to a unimodal distribution. From Figure 6a, it can also be observed that the small diameter mode slightly increased in particle size from 650 °C to 1000 °C. This is because more precursors evaporate from large particles at higher temperature, which leads to increased homogeneous nucleation of smaller particles. Higher vapor and particle concentrations promote faster particle growth and coagulation, thus the particle size increased slightly.

Figure S3 shows the influence of the furnace temperature, the precursor component concentration and aerosol flow rate on the geometric mean diameter of as-synthesized powders. The particle size is increasing with increase in temperature as discussed above. Increasing concentration also increases the GMD of the nanoparticles due to a greater number of solutes within one droplet.

However, the final particle size is not proportional to cubic root of the precursor concentration, as in Equation 4, because of a partial gas-to-particle mechanism. Surprisingly, the particle size increases with increasing the flow rate. This is attributed to the design of the Collison nebulizer. In our experimental system, the flow rate is modified by controlling the gas pressure entering the nebulizer chamber, which will change the number concentration and size distribution of initial droplets simultaneously. Although the residence time decreases, a higher number concentration at a larger flow rate results in more collision and coagulation.

From what has been discussed above, the particle size distribution can be controlled by changing the furnace temperature, the flow rate and the precursor concentration. Only under certain conditions, powders with high purity can be synthesized. We successfully fabricated perovskite oxides with high purity for the precursor concentration 0.05M, 0.025M and 0.01M. The particle size distributions are shown in Figure 6b. It can be observed that the particle size increases with increasing concentration and temperature. The GMD for highly pure powders at 0.05M, 0.025M, 0.01M are 33.96, 38.60 and 47.33nm, respectively.

Figure S4 shows a TEM image of single-phase perovskite $KBaTeBiO_6$ synthesized under the optimum conditions (barium concentration: 0.025 M, K:Ba:Te:Bi=1:1:1:0.8, furnace temperature: 900 °C, the aerosol flow rate: 1.8 L min^{-1}). There are two type of nanoparticles, small one and large one. Large irregular nanoparticles are generated through the droplet-to-particle route, whereas the small agglomerates result from the gas-to-particle pathway. The morphology of large nanoparticles is not solid sphere as expected. In contrast, the powders have irregular shapes. This may be because of the low melting and boiling temperate of metal nitrates.[39] Under the high temperature in the furnace, the nitrate salts melt, boil and evaporate before the decomposition, which leave pores inside the particle. Then those pores are removed in the cooling stage, which result in irregular solid particles. It was also found that the operation parameters, such as the furnace temperature, aerosol flow rate and the precursor concentration have little influence on the particle morphology. All of them result in irregular shapes. HR-TEM was further performed to confirm the crystal structure, indicating high crystallinity of as-prepared nanoparticles.

The UV–visible absorption spectra of phase pure powders are shown in Figure 7. It indicates the fundamental absorbance stopping wavelength at 354 nm. It cannot absorb visible light due to the wide bandgap.

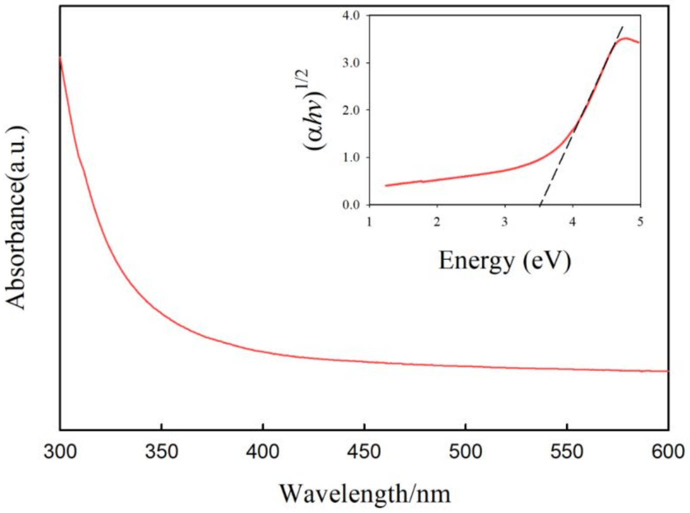

Figure 7. UV-vis of phase-pure perovskite oxide $KBaTeBiO_6$ synthesized by FuAR

The inset of Figure 7 plots $(ah\nu)^{1/2}$ as a function of energy. Based on Tauc method, the indirect band gap of $KBaTeBiO_6$ is calculated to be 3.5 eV, which is different from the theoretically predicted value of 1.94 eV by DFT, and of those obtained using wet-chemistry.[9] This is because the actual cation ratio of the as-prepared perovskites is 0.4:1.6:1.14:0.86 from ICP-OES data, rather than 1:1:1:1 used in the DFT calculation. From previous report,[17] it concluded that the chemical composition plays a significant role in determining the bandgap. Bi-rich composition can significantly reduce the bandgap. However, in this study, to eliminate the bismuth oxide impurities and obtain the phase pure perovskite, the bismuth content was reduced. According to the ICP-OES result, Bi/Ba is 0.5 far less than 1 which is used for DFT calculations. Therefore, the bandgap of phase pure perovskite synthesized in FuAR is raised from 1.94 eV to 3.5 eV. This also indicates that the huge bandgap of the furnace made $KBaTeBiO_6$ may be tuned to the narrow bandgap for efficient utilization of solar spectrum in future.

3.3. CO_2 photoreduction

The wide band gap of as-synthesized perovskites limits its applications in photovoltaics. However, semiconductor materials with wide band gap are possible to be used as photocatalysts for CO_2 reduction in the presence of water vapor.[40,41] The photocatalytic performance of phase pure double perovskite oxides synthesized by FuAR was investigated in our experimental system as described above. Prior to that, control tests were conducted under the following five conditions: (1) glass filter without catalysts; (2) no light illumination; (3) no CO_2 and H_2O with light illumination; (4) only introducing CO_2 with light illumination; (5) only introducing H_2O with light illumination. No hydrocarbons are detected by the GC under these five cases, which indicates the absence of CO_2 photoreduction. However, in the presence of all catalysts, CO_2 and H_2O, and light illumination, CO was detected. The results show that CO is produced by the photoreduction of CO_2 and H_2O, instead of decomposition of surface carbon residue on the catalyst.

It was found that CO was the main product in our flow reaction system. The mechanism of photoreduction of CO_2 is quite complex and still in a controversy, single-electronic versus multi-electronic processes. Many researchers[42, 43] believe that the photoreduction of CO_2 is based on the proton-assisted multi-electron transfer mechanism (MET) rather than single electron transfer, because the high photoreduction potential for a single-electronic process of $CO_2 + e^- \rightarrow CO_2^{\cdot -}$ $(E^0 = -1.90\ V\ vs.\ NHE)$ is unfavorable compared to redox potential of -0.2-0.8 V for the multi-electron process. Based on MET mechanism, the conversion of CO_2 requires multiple electrons and a corresponding number of protons participating. The products could be different depending on the number of electrons and protons. To produce CH_4, it requires 8 electrons and 8 H atoms on the same catalysts, while the formation of CO only needs two electrons and protons. CO as the main product on the gas-solid interface in many previous studies[25,27,44] is possible due to the lack of protons. In contrast to that, CH_4 and other hydrocarbons are often obtained in aqueous solutions for CO_2 photoreduction possible due to more protons provided by water.[45,46] In addition, one plausible pathway for the formation of CH_4 is: $CO_2 \rightarrow CO \rightarrow CO_2^{\cdot -} \rightarrow CH_2 \rightarrow CH_4$.[47-49] The desorption of CO from the surface before it fully reduced can also limit the formation of CH_4. All these above-mentioned reasons make it more difficult to produce CH_4 than CO on the gas-solid interface. Therefore, CO was found as the main product in our reaction system.

CO_2 photoreduction experiments were repeated four times using fresh samples. The average CO production rates with the standard derivation versus the irradiation time for 3 h are shown in the Figure 8a. It can be observed that the CO yield achieved the highest value of ~ 180 μmol g^{-1} h^{-1} in the first half hour. However, it gradually decreased with reaction time after the optimal value. In the last half hour, the CO production rate is around 25 μmol g^{-1} h^{-1}.

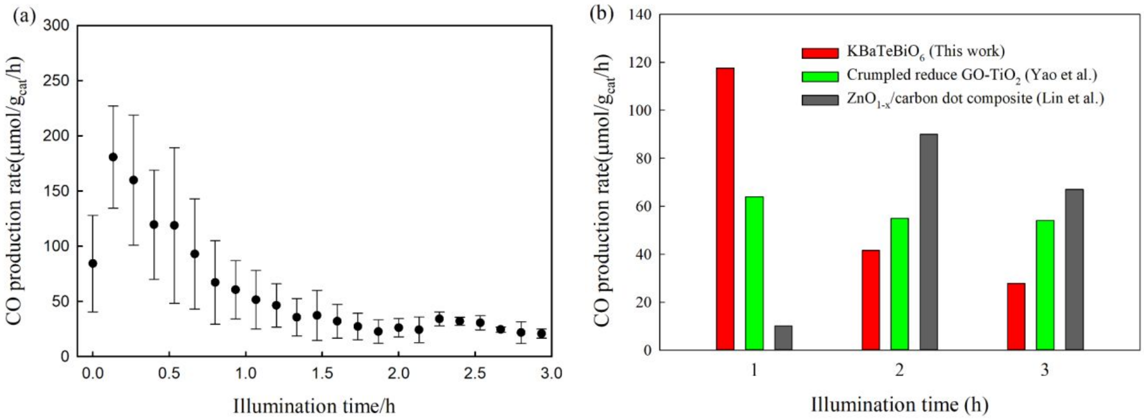

Figure 8. a) Average CO production rate as a function of illumination time; b) The comparison of average CO production rate between $KBaTeBiO_6$ (this work), ZnO_{1-x}/C (Lin et al.[36]), and EDA-rGO-TiO_2 (Yao et al. [37])

The initial high catalytic performance is likely attributed to the unique properties and structure of perovskites. For $KBaTeBiO_6$ perovskite oxides, K and Ba occupy A sites, while B sites host Te and Bi cations. B site cations and oxygen anions form corner-sharing BO_6 octahedra. Using alkali or alkaline-earth metals such as K and Ba as the A-site cations is beneficial to the CO_2 adsorption according to Lewis acidity of CO_2. B site cations play a key role in the electronic structures. Thind et al.[9] employed DFT calculation to simulate the electronic structures of $KBaTeBiO_6$. They found that the valence band is mainly comprised of O 2p and Bi 6s states with a small fraction of Te 4d states, whereas the conduction band predominately consists of Bi 6p and Te 5s states. The presence of Bi 6s orbitals in the valence band is likely to reduce the bandgap.[50] In addition, DFT studies show that the heavy Bi^{3+} cation with its 6p state leads to a widely dispersed band with a low effective mass of the electrons and holes, thus improving the electron transfer and CO_2 reduction.

To understand the CO_2 photoreduction in depth, the band diagram of the as prepared perovskite was constructed by performing UV-vis spectra and UPS measurement. The optical band gap was determined to be 3.5 eV from the Tauc plot. The valence band maximum (VBM) with respect to the vacuum level was determined to be -6.8 eV, as seen in Figure 9a. Conduction band minimum (CBM) was calculated to be -3.3 eV with respect to the vacuum level by using the measured bandgap and VBM. The constructed band diagram of the as-synthesized

$KBaTeBiO_6$ is shown in Figure 9b, where the CBM and VBM position corresponded to -1.2 and 2.3 eV versus the normal hydrogen electrode (NHE) at pH 0. That is, the CBM is more negative than the reduction potential of $E^0(CO_2/CO) = -0.52\ V\ vs.\ NHE$; the VBM is more positive than the oxidation potential of $E^0(O_2/H_2O) = 0.82\ V\ vs.\ NHE$, indicating a good band alignment for CO_2 photoreduction.[51]

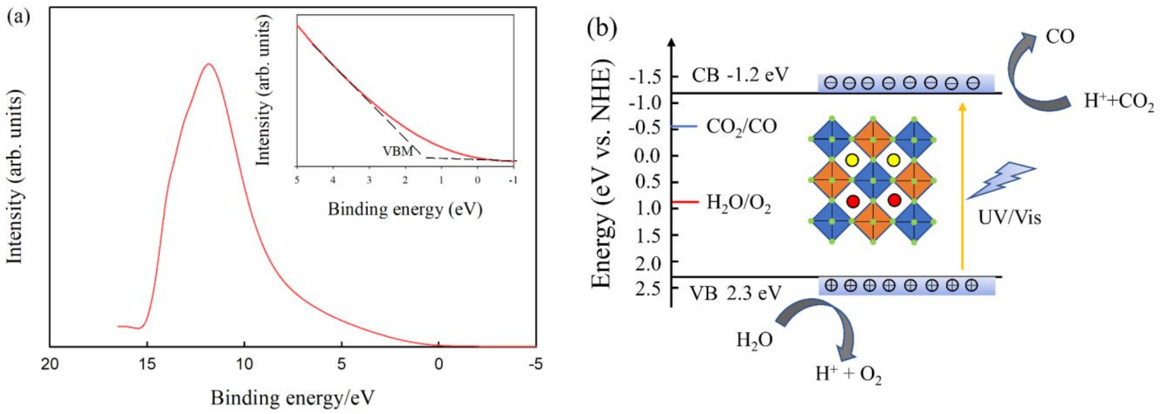

Figure 9. a) Valence band characterization by UPS; b) The band diagram of as-synthesized perovskite for CO_2 photoreduction

The surface compositions of fresh sample and spent catalysts were characterized by XPS, as shown in Figure S5 (see the supporting information). Figure S5a shows a typical survey XPS spectrum of fresh sample with high purity, where the signal of potassium(K), barium (Ba), bismuth (Bi), tellurium (Te) and oxygen (O) are obviously identified. A carbon peak is also detected, which is likely attributed to adventitious carbon contamination. Considering the synthesis process performed in the air, the adventitious carbon contamination is unavoidable. To further investigate the carbon peak before and after photoreduction, high-resolution C 1s spectra of fresh samples and spent catalysts are shown in Figure S5b. The deconvolution of the C 1s spectra for the fresh sample only yields one peak at 284.8 eV, which originated from contamination carbon (C-C). There is no any component of carbonate at higher binding energy. The deconvolution of the C 1s of the spent catalysts shows two strong peaks at 284.8 eV and 288.5 eV, which are assigned to adventitious carbon contamination and carbonate, respectively.

This is consistent with XRD results, as seen in Figure S6. Compared to the fresh sample, the used one shows a significant secondary phase, which corresponds to barium carbonate ($BaCO_3$). Carbonates are only generated after photoreduction. Before the reaction, the fresh samples don’t contain surface carbonates. This further confirm the CO is from the CO_2, not from the surface carbonate prior to catalysis.

The surface chemistries of the catalyst exposure to only CO_2 and only H_2O were also investigated by XPS. From Figure S5c, it can be observed that carbonate CO_3^{2-} is formed even only introducing CO_2 into the reactor. The surface CO_3^{2-} is formed possible due to CO_2 molecules bonded to the surface oxygen atom through its carbon atom.[52] The CO_3^{2-} as active intermediate is able to form CO by reacting with the protons generated from H_2O.[53–55] However, due to the absence of H_2O, there is no CO producing. There is no obvious change for catalyst only exposure to H_2O as shown in Figure S5c and S5d, indicating a good stability of perovskite oxide under humid environment.[9]

From what has been discussed above, we can conclude a plausible pathway for CO_2 photoreduction in our reaction system, as shown in Figure 9b. The as-synthesized $KBaTeBiO_6$ is illuminated by UV light and then generated electron-hole pairs by absorbing photons whose energy is above the bandgap. A mixture of CO_2 and H_2O diffuses and then absorbs onto the surface of the catalysts. Water could be oxidized into hydrogen ions (H^+), which is used for reduction of CO_2. CO_2 is bonded to the surface oxygen atom to form the carbonate species, which then react with protons generated from H_2O to produce CO.

Since barium carbonates are produced during the reaction, it is believed that the decreasing performance could be due to the coverage and saturation of the active sites by the new generated carbonate layers. Literatures showed that the accumulation of carbonaceous intermediates on the surface of catalysts could lead to the coverage of active sites and thus induced the deactivation.[53, 56-57] Because barium is possible leaching and reacting with CO_2, the barium elements can be replaced by other elements such as Li to improve the stability.[58] Optimization strategies are in progress to enhance the catalytic stability of the as-synthesized samples for CO_2 photoreduction.

In spite of the poor stability of as-synthesized samples, the high average CO production rate of 180 μmol g^{-1} h^{-1} in the first half hour demonstrated a superior photocatalytic efficiency to those of most reported perovskite photocatalysts in literature, whose production rates are commonly on the order of nmol g^{-1} h^{-1} (see Table S3). We also compared our samples with other typical semiconductors published in our group[25,26] using the same reactor system. The results are shown in Figure 8b, which indicates a compared efficiency of our samples to other catalysts. The quantum efficiency based on CO yield was calculated to be 1.19 % after irradiation for 60 min under UV–vis light (see Supporting information for details), which is around 10, and 125 times higher than reported for ZnO_{1-x}-C (0.13%), and EDA-rGO-TiO_2 (0.0094%), respectively.

4. Conclusion

A novel double perovskite oxide with nominal composition $KBaTeBiO_6$ was rapidly synthesized in a single step process in a furnace aerosol reactor (FuAR). Various studies conducted allowed us to develop a firm relationship of precursor concentrations and operating parameters to obtain the desired perovskite phase. The perovskite phase formation mechanism was established to allow choosing the necessary temperature and residence time for the synthesis process in FuAR. Then, nanosized perovskite oxides with high purity were fabricated by controlling the operation parameters. The effects of the furnace temperature, the aerosol flow rate, and the precursor component concentration on particle size, morphology and phase purity were investigated systematically. It was found that there is a temperature window within which the sample has the desired crystal phases. The phase pure perovskite oxide $KBaTeBiO_6$ was obtained under a specific combination of operation conditions (900 °C, 1.8 L min^{-1}, K:Ba:Te:Bi=1:1:1:0.8, 0.025 M). Moreover, the particle formation mechanism in the furnace aerosol reactor was identified to be a combination of gas-to-particle and droplet-to-particle pathways. The geometric mean diameter of particles increased with the increase in furnace temperature, flow rate and initial precursor concentration. The operation conditions were found to have little influence on the morphology of nanoparticles. The phase pure perovskite oxide $KBaTeBiO_6$ was then employed as a photocatalyst for CO_2 reduction. The average CO production rate was found to be 180 μmol g^{-1} h^{-1} in the first half hour, higher than many conventional semiconducting oxide catalysts. The photoreduction rate was found to decrease with time due to the formation of an inert $BaCO_3$ layer. However, the existence of a minor second phase was found to decrease the photocatalytic performance. Optimization strategies are currently in progress to enhance the catalytic stability of the as-synthesized samples for CO_2 photoreduction.

Supporting Information
Supporting Information is available from the author.

Acknowledgements

The work was partially supported by the National Science Foundation, through awards DMR-1806147 and CBET-1705864

Conflict of Interest

The authors declare no conflict of interest.

References

[1] J. Hwang, R. R. Rao, L. Giordano, Y. Katayama, Y. Yu, Y. Shao-Horn, *Science* **2017**, 358, 751.

[2] X. Xu, Y. Zhong, Z. Shao, *Trends in Chemistry* **2019**, 1, 410.

[3] W.-J. Yin, B. Weng, J. Ge, Q. Sun, Z. Li, Y. Yan, *Energy & Environmental Science* **2019**, 12, 442.

[4] S. Afroze, A. Karim, Q. Cheok, S. Eriksson, A. K. Azad, *Frontiers in Energy* **2019**, 1.

[5] M. T. Anderson, K. B. Greenwood, G. A. Taylor, K. R. Poeppelmeier, *Progress in solid state chemistry* **1993**, 22, 197.

[6] G. King, P. M. Woodward, *Journal of Materials Chemistry* **2010**, 20, 5785.

[7] S. Vasala, M. Karppinen, *Progress in solid state chemistry* **2015**, 43, 1.

[8] F. Faber, A. Lindmaa, O. A. von Lilienfeld, R. Armiento, *Bulletin of the American Physical Society* **2017**, 62.

[9] A. S. Thind, S. Kavadiya, M. Kouhnavard, R. Wheelus, S. B. Cho, L.-Y. Lin, C. Kacica, H. K. Mulmudi, K. A. Unocic, A. Y. Borisevich, *Chemistry of Materials* **2019**, 31, 4769.

[10] M. H. Rubel, T. Takei, N. Kumada, M. M. Ali, A. Miura, K. Tadanaga, K. Oka, M. Azuma, M. Yashima, K. Fujii, *Chemistry of Materials* **2016**, 28, 459.

[11] L. Zhou, Y. F. Xu, B. X. Chen, D. B. Kuang, C. Y. Su, *Small* **2018**, 14, 1703762.

[12] Z. Sun, Z. Yang, H. Liu, H. Wang, Z. Wu, *Applied surface science* **2014**, 315, 360.

[13] W. Dai, J. Yu, H. Xu, X. Hu, X. Luo, L. Yang, X. Tu, *CrystEngComm* **2016**, 18, 3472.

[14] E. T. McClure, M. R. Ball, W. Windl, P. M. Woodward, *Chemistry of Materials* **2016**, 28, 1348.

[15] A. H. Slavney, T. Hu, A. M. Lindenberg, H. I. Karunadasa, *Journal of the American chemical society* **2016**, 138, 2138.

[16] M. R. Filip, S. Hillman, A. A. Haghighirad, H. J. Snaith, F. Giustino, *The journal of physical chemistry letters* **2016**, 7, 2579.

[17] W.-N. Wang, W.-J. An, B. Ramalingam, S. Mukherjee, D. M. Niedzwiedzki, S. Gangopadhyay, P. Biswas, *Journal of the American chemical society* **2012**, 134, 11276.

[18] M. S. Sheikh, A. P. Sakhya, R. Maity, A. Dutta, T. Sinha, *Solar Energy Materials and Solar Cells* **2019**, 193, 206.

[19] B. Chu, H. An, X. Chen, Y. Cheng, *Applied Catalysis A: General* **2016**, 524, 56.

[20] Y. Chen, J. Shen, G. Yang, W. Zhou, Z. Shao, *Journal of Materials Chemistry A* **2017**, 5, 24842.

[21] D. Burnat, A. Heel, L. Holzer, D. Kata, J. Lis, T. Graule, *Journal of Power Sources* **2012**, 201, 26.

[22] D. D. Athayde, D. F. Souza, A. M. Silva, D. Vasconcelos, E. H. Nunes, J. C. D. da Costa, W. L. Vasconcelos, *Ceramics International* **2016**, 42, 6555.

[23] M. M. Bućko, J. Obłąkowski, *Journal of the European Ceramic Society* **2007**, 27, 3625.

[24] A. Coats, J.-P. Redfern, *Journal of Polymer Science Part B: Polymer Letters* **1965**, 3, 917.

[25] L.-Y. Lin, S. Kavadiya, B. B. Karakocak, Y. Nie, R. Raliya, S. T. Wang, M. Y. Berezin, P. Biswas, *Applied Catalysis B: Environmental* **2018**, 230, 36.

[26] Y. Nie, W.-N. Wang, Y. Jiang, J. Fortner, P. Biswas, *Catalysis Science & Technology* **2016**, 6, 6187.

[27] W.-N. Wang, J. Park, P. Biswas, *Catalysis Science & Technology* **2011**, 1, 593.

[28] H. Zhang, M. T. Swihart, *Chemistry of materials* **2007**, 19, 1290.

[29] H. E. Kissinger, *Journal of research of the National Bureau of Standards* **1956**, 57, 217.

[30] K. Cho, H. Chang, D. S. Kil, J. Park, H. D. Jang, H. Y. Sohn, *Aerosol Science and Technology* **2009**, 43, 911.

[31] K. Y. Jung, J. H. Lee, H. Y. Koo, Y. C. Kang, S. B. Park, *Materials Science and Engineering: B* **2007**, 137, 10.

[32] P. Biswas, C. Y. Wu, *Journal of the Air & Waste Management Association* **1998**, 48, 113.

[33] T. T. T. Kodas, M. J. Hampden-Smith, *Aerosol processing of materials*, Wiley-Vch, **1999**.

[34] K. T. Jacob, Y. Waseda, (1988), *Journal of the Less Common Metals* **1988**, 139, 249.

[35] L. S. Brooks, *Journal of the American Chemical Society* **1952**, 74, 227.

[36] A. K. Fischer, *The Journal of Chemical Physics* **1966**, 45, 375.

[37] E. F. Fiock, W. H. Rodebush, *Journal of the American Chemical Society* **1926**, 48, 2522.

[38] W.-N. Wang, Y. Jiang, P. Biswas, *The journal of physical chemistry letters* **2012**, 3, 3228.

[39] G. L. Messing, S. C. Zhang, G. V. Jayanthi, *Journal of the American Ceramic Society* **1993**, 76, 2707.

[40] H. Zhou, P. Li, J. Guo, R. Yan, T. Fan, D. Zhang, J. Ye, *Nanoscale* **2015**, 7, 113.

[41] T. Inoue, A. Fujishima, S. Konishi, K. Honda, *Nature* **1979**, 277, 637.

[42] A. J. Morris, G. J. Meyer, E. Fujita, *Accounts of chemical research* **2009**, 42, 1983.

[43] A. H. Yahaya, M. A. Gondal, A. Hameed, *Chemical physics letters* **2004**, 400, 206.

[44] L.-Y. Lin, Y. Nie, S. Kavadiya, T. Soundappan, P. Biswas, *Chemical Engineering Journal* **2017**, 316, 449.

[45] X. H. Xia, Z. J. Jia, Y. Yu, Y. Liang, Z. Wang, L. L. Ma, *Carbon* **2007**, 45, 717.

[46] I. H. Tseng, W. C. Chang, J. C. Wu, *Applied Catalysis B: Environmental* **2002**, 37, 37.

[47] C. Huang, Z. Li, Z. Zou, *MRS Communications* **2016**, 6, 216.

[48] W. Tu, Y. Zhou, Z. Zou, *Advanced Materials* **2014**, 26, 4607.

[49] G. R. Dey, *Journal of natural gas chemistry* **2007**, 16, 217.

[50] J. Tang, Z. Zou, J. Ye, *The Journal of Physical Chemistry C* **2007**, 111, 12779.

[51] R. Shi, G. I. Waterhouse, T. Zhang, *Solar Rrl* **2017**, 1(11), 1700126.

[52] Y. Wang, J. Zhao, Y. Li, C. Wang, *Applied Catalysis B: Environmental* **2018**, 226, 544.

[53] L. Y. Lin, S. Kavadiya, X. He, W. N. Wang, B. B. Karakocak, Y. C. Lin, M. Y. Berezin, P. Biswas, *Chemical Engineering Journal* **2020**, 389, 123450.

[54] E. Karamian, S. Sharifnia, *Journal of CO2 Utilization* **2016**, 16, 194.

[55] C. Luo, J. Zhao, Y. Li, W. Zhao, Y. Zeng, C. Wang, *Applied Surface Science* **2018**, 447, 627.

[56] D. Uner, M. M. Oymak, *Catalysis today* **2012**, 181, 82.

[57] L. Liu, C. Zhao, J. T. Miller, Y. Li, *The Journal of Physical Chemistry C* **2017**, 121, 490.

[58] B. Han, M. Risch, Y. L. Lee, C. Ling, H. Jia, Y. Shao-Horn, *Physical Chemistry Chemical Physics* **2015**, 17, 22576.